



Mechanical-Activated Digital Microfluidics with Gradient Surface Wettability

Journal:	<i>Lab on a Chip</i>
Manuscript ID	LC-ART-09-2018-000976.R1
Article Type:	Paper
Date Submitted by the Author:	30-Nov-2018
Complete List of Authors:	Qi, Lin; The Ohio State University, Biomedical Engineering Niu, Ye; The Ohio State University, Department of Biomedical Engineering; The Ohio State University, Department of Mechanical and Aerospace Engineering Ruck, Cody; Barnes and Noble at The Ohio State University Official Bookstore, Department of Biomedical Engineering Zhao, Yi; The Ohio State University,

Mechanical-Activated Digital Microfluidics with Gradient Surface Wettability

Lin Qi^{1#}, Ye Niu^{1,2#}, Cody Ruck¹, and Yi Zhao^{1*}

¹Department of Biomedical Engineering, The Ohio State University, Columbus OH 43210

²Department of Mechanical and Aerospace Engineering, The Ohio State University,
Columbus OH 43210

#: The authors contribute equally to this paper.

*: To whom all correspondence should be addressed: zhao.178@osu.edu

Abstract

This paper reports a simple yet effective droplet manipulation approach that can displace aqueous droplets over a long distance within the working plane. Repeated patterns with surface gradient wettability were created on a super-hydrophobic surface by laser irradiation. Aqueous droplets as small as $2 \mu\text{L}$ are moved on the patterns over a long distance under in-plane symmetric cyclic vibration. Typical droplet manipulation actions including droplet movement along a pre-determined trajectory, droplet mixing, and selective movement of multiple droplets were successfully demonstrated. Biochemical detection using this approach was demonstrated via a bicinchoninic acid (BCA) assay. This approach allows for long-distance droplet movement and simultaneous manipulation of multiple droplets without sacrificing the manipulation efficiency or increasing the cross-contamination risk. The device can be fabricated outside cleanrooms and operated without special equipment. It provides a solid technical basis for developing the next generation of affordable open channel microfluidic devices for various applications.

Introduction

In the past two decades, microfluidics that allows for biochemical reactions with minute sample consumptions has been employed broadly in various fields^{1, 2}. Different from the conventional closed-channel microfluidics with continuous flow, droplet-based microfluidics has received extraordinary attention due to reduced biomolecule adsorption and low risk of cross-contamination³⁻⁶. In droplet-based microfluidics (also known as digital microfluidics), liquid droplets with various chemicals can be isolated from or mixed with each other on demand. Each droplet with microliters in volume can serve as an individual microreactor. The stand-alone droplet reservoirs make it possible to implement high-throughput examinations with reduced reagent consumption and small device footprint^{7, 8}. Among multitudinous droplet-based microfluidics designs, open-channel microfluidics has several distinct advantages. It is free from the reliance on excessive driving fluids and complicated pumping units. The entire working surface can be utilized to host a large number of droplet moving trajectories. Also, the leaking issue in closed-channel microfluidics is no longer a concern.

In open-channel microfluidics, liquid droplets can be manipulated by various physical means. Electrowetting-on-dielectric (EWOD) is a popular technique for droplet actuation⁹, where droplet motion is induced by creating a wettability difference between the front and the rear edges of a droplet by the electrowetting effect. Typical microfluidic functions including linear droplet translocation, merging, and mixing were successfully demonstrated¹⁰⁻¹³. Nonetheless, EWOD is limited by possible electrical breakdown¹⁴. A droplet with high ionic concentration can significantly decrease the breakdown voltage and cause irreversible failure of EWOD chips^{15, 16}. Dielectrowetting has been recently reported to completely eliminate the direct contact between the ionic droplet and electrodes¹⁷. Non-electrical droplet manipulation approaches have also been developed¹⁸⁻²⁵. Among numerous non-electrical stimulation

approaches, mechanical means with relatively simple setup and high process flexibility exhibit a promising potential²²⁻²⁷. Droplet can be driven by applying asymmetric in-plane vibration^{25, 28}, dynamically tilting the working substrate²⁷, or deforming the local surface²⁴. Droplet can also be moved towards the more wettable area on a surface with anisotropic wettability, either spontaneously²⁹ or with the help of mechanical agitation³⁰⁻³². In addition, the droplet can translocate under vertical vibration along an anisotropic ratchet conveyor that consists of periodic asymmetric textures or alternating hydrophilic and hydrophobic arcs³³⁻³⁵. Once the vertical vibration is applied, the contact line of the droplet oscillates. The contact line experiences an asymmetric drive force toward one direction during the de-wetting process, which allows the droplet to slide. Although these mechanical stimulation approaches are intriguing, broad adoption of these approaches is hindered by several limitations. In particular, the manipulation using asymmetric vibration can only manipulate droplets within a narrow size range at the same time²⁵. It is challenging to move multiple droplets of different sizes simultaneously or selectively moving some droplets while keeping others of the same size stationary. In the approaches using anisotropic wettability, the wettability gradient must be sufficiently large to overcome the contact angle hysteresis under mechanical interferences. This, however, limits the traveling distance^{31, 32}. In the approaches that use vertical vibration to move droplets on asymmetric surface textures, the droplets may be subject to the off-contact from the substrate³⁶, especially when a high frequency is used to manipulate small droplets. The hydrophilic surface in the arcs raises the risks of undesired satellite droplets formation and surface contamination³⁷.

In this study, an alternative mechanical stimulation approach for open-channel digital microfluidics is presented. Repeated patterns with gradient surface wettability are printed on a super-hydrophobic working substrate by laser engraving. The patterns are arranged head-to-

tail into a linear cascade (**Fig. 1a**). The surface wettability gradient in each pattern aligns along the longitudinal axis of the pattern. Different from previous studies where a droplet on a gradient wettability surface moves towards the more hydrophilic side under mechanical agitation, the droplet in this approach moves towards the more hydrophobic part of the same pattern, across the pattern boundary, and reaches the more hydrophilic part of the next pattern. This is due to the head-to-tail arrangement of the repeated patterns, which sets a sharp difference of wettability gradient at the two edges of the droplet. Continuous vibration leads to a large droplet displacement. This approach allows droplets to move over a long distance not limited by the pattern length. Since the droplet moving threshold varies with both the pattern width and the droplet volume, selective droplet movement is possible. All the areas on the working substrate are within the hydrophobic regime where the static contact angle is greater than 125° . The risks of undesired satellite droplets formation and cross-contamination are thus reduced.

Materials and Methods

Working principle

A 2D model was established to investigate the droplet motion (**Fig. 1a**). Assuming the gradient of the surface wettability is sufficiently high, the droplet dispensed on the pattern can move spontaneously to the more hydrophilic edge of the pattern due to the contact angle hysteresis. Once the in-plane vibration is applied, the droplet is subject to the inertial force induced by vibration and the drag force from contact angle hysteresis. The inertial force can be expressed as $F_{inert} = mA_0(2\pi f)^2 \sin 2\pi ft$, where m is the droplet mass, A_0 is the vibration amplitude which is constant in this study, and f is the vibration frequency. It is seen that F_{inert} increases with the vibration frequency f . Under a small f , F_{inert} cannot overcome the contact angle hysteresis so that the droplet keeps stationary. Once f exceeds a certain threshold (at point M

in **Fig. 1b&c**), F_{inert} overcomes contact angle hysteresis. The droplet starts to accelerate, as described by:

$$F_{inert} - \gamma C w (\cos \theta_r - \cos \theta_a) = m \frac{d^2 x}{dt^2} \quad (1).$$

The second term on the left of **Eqn. 1** $\gamma C w (\cos \theta_r - \cos \theta_a)$ refers to the drag force, where γ is the surface tension of water/air interface, C is a shape-correction coefficient related to the geometry of the contact line between the droplet and the substrate, w is the pattern width, θ refers to the dynamic contact angles, and the subscripts a and r refer to the advancing edge and the receding edge of the droplet, respectively. Assuming both the leading edge and the trailing edge are semi-circular, C is approximated as ~ 1.57 . Here, the viscous dissipation near the rim of the contact lines and that in bulk as well as the energy dissipation due to pinning/de-pinning of the contact lines are neglected. This is because they are at least one order of magnitude lower than the energy loss due to contact angle hysteresis. A detailed estimation is provided in Section 1 in electronic supplementary information (ESI).

For analysis simplicity, the moving directions and the dynamic contact angles at both edges of the droplet are defined. The direction towards positive contact angle gradient (pointing from the more hydrophilic edge of a pattern to the more hydrophobic edge of the same pattern) is defined as the forward direction (the right direction in **Fig. 1a**). The opposite direction is defined as the backward direction. Assuming that the dynamic contact angle within a pattern changes linearly along the longitudinal axis of the pattern, the advancing angle of a droplet within the pattern can be expressed as $\theta_a(x) = \theta_{a,phi} + \frac{x}{L}(\theta_{a,pho} - \theta_{a,phi})$, where L is the length of a pattern, the subscript *phi* refers to the more hydrophilic edge of the pattern, and the subscript *pho* refers to the more hydrophobic edge of the same pattern. Similarly, the receding angle can be expressed as $\theta_r(x) = \theta_{r,phi} + \frac{x}{L}(\theta_{r,pho} - \theta_{r,phi})$.

When the substrate moves to the left with a frequency exceeding a certain threshold, the droplet accelerates towards the forward direction:

$$F_{inert} - \gamma C w \left[\cos \left(\theta_{r,phi} + \frac{\theta_{r,pho} - \theta_{r,phi}}{L} x \right) - \cos \left(\theta_{a,phi} + \frac{\theta_{a,pho} - \theta_{a,phi}}{L} (x + d) \right) \right] = m \frac{d^2 x}{dt^2} \quad (2),$$

where x is the position of the receding edge, and d is the distance between the advancing edge and receding edge. The droplet displacement within $0 < t \leq T/2$ (as illustrated by the dark grey area in **Fig. 1b&c**) can be derived by solving **Eqn. 2** with the conditions of $x=0$ @ $t=0$ and $\frac{dx}{dt} = 0$ @ $t = 0$, where $T = \frac{1}{f}$ is the vibration period.

After $T/2$ (point N in **Fig. 1b&c**), the inertial force points to the backward direction ($F_{inert} < 0$), while the drag force still points to the backward direction until the droplet velocity ceases to zero. If the droplet velocity can reach zero at the moment of T_0 before the completion of a full period ($T_0 < T$), the displacement of the droplet within $\frac{T}{2} < t \leq T_0$ (the light grey area in **Fig. 1b&c**) can be derived by solving **Eqn. 2** using the values of $x(\frac{T}{2})$ and $\frac{dx}{dt}(\frac{T}{2})$ determined from the first half period. If the droplet displacement at T_0 (point O) is smaller than the pattern length L (as in **Fig. 1b**), the droplet moves towards the backward direction after T_0 and is not able to reach the next pattern (**Fig. 1b**). If the droplet displacement at T_0 equals or is greater than L , the droplet reaches the next pattern. After T_0 , the drag force points to the forward direction. Since the advancing edge of the droplet now sits at the more hydrophobic edge of the previous pattern while the receding edges sits at the more hydrophilic side of the current pattern, the drag force is much greater than that in the first half period. If the drag force is sufficiently large to prevent the droplet from returning to the previous pattern, the droplet can be displaced by a pattern length within one cycle (**Fig. 1c**). The minimal vibration frequency that meets this condition is denoted as f_{min} . If the inertial force towards the backward direction

is greater than the high drag force while the droplet resides at the more hydrophilic edge of the current pattern:

$$F_{inert} > \gamma C W \left[\cos \left(\theta_{r,phi} + \frac{\theta_{r,pho} - \theta_{r,phi}}{L} d \right) - \cos(\theta_{a,pho}) \right] \quad (3),$$

the droplet can return to the previous pattern. The minimal frequency associated with this condition is denoted as f_{max} . Beyond this frequency, the droplet may move across the pattern boundaries along both forward and backward directions, resulting in random motions. Therefore, f_{max} is the maximally allowed frequency for controlled unidirectional droplet movement. It should be noted that if the driving frequency continues to increase to an extremely large value, the droplet may exhibit vibrations on the surface with a small amplitude. This is because the damping effect caused by viscosity dissipation become predominant.

Based on the model, the range of vibration frequency that can cause controlled unidirectional droplet displacement on the repeated patterns with gradient wettability was determined. Given the material, physical and geometric parameters of droplets and the substrate in this study, the frequency that can displace a $20 \mu L$ droplet over a pattern is calculated as 8.9~18.2 Hz. With continuous vibration under a frequency within the range, long-distance droplet movement can be achieved.

The droplet motion can be better understood through an analogy to the motion of a solid sphere on a substrate with repeated saw-toothed topography (**Fig. 1d**), where the surface wettability gradient is in analogy to the slope of each saw-toothed pattern; the high wettability barrier at the pattern boundary is in analogy to height difference at the boundary of two adjacent saw-toothed patterns; and the surface energy of the gradient wettability substrate is in analogy to the potential energy of the solid sphere. The in-plane vibration applies an inertial force on the sphere towards opposite lateral directions. The minimal inertial force that can move the sphere

on the slope wall is lower than that can have the sphere climb over the vertical wall at the pattern boundary. As a result, the droplet moves towards the forward direction if frequency reaches a certain threshold (right in **Fig. 1d**). Similar as in the droplet motion, the sphere can travel the distance of a pattern length in each cycle. Long-distance traveling can be achieved by continuous vibration.

Substrate preparation

A PDMS (Sylgard 184, Dow Corning, MI) substrate was fabricated by mixing a base pre-polymer and a curing agent at the weight ratio of 10:1. The pre-polymer solution was then degassed in vacuum for 30 *min* and dispensed on a petri dish surface to achieve a 2 *mm* thick PDMS layer. The solution was cured on a hot plate at 65°C for 2 *hours*. A super-hydrophobic layer (Rust-Oleum NeverWet, IL, USA) was spun on the PDMS substrate at 6000 *rpm*. The substrate was placed in a ventilation cabinet for 3 *hours* for solvent evaporation and cut into rectangular pieces (70 *mm* × 30 *mm*) before use.

Laser irradiation

The gradient surface wettability was created on the PDMS substrate using laser irradiation with spatially varied laser dose (25 *W*, VSL2.30, Universal Laser Systems, AZ) (**Fig. 2a**). The laser was operating in air. The change of surface hydrophobicity is due to the laser induced change of both surface topography and surface chemistry (Section 2 in ESI). The laser dose was changed by altering three operating parameters (Gray Scale (*GS*), Raster Intensity (*RI*) and the engraving cycles (*n*)) as elaborated in a previous report³⁸. Briefly, *GS* and *RI* allow independent control of the laser power in temporal and spatial domains, and *n* determines the total laser dose. Other operating parameters, including the laser spot size (~127 μm), the lateral traveling speed of the laser head (0.2629 *m/s*), the laser repetition rate (5000 *Hz*), and the spatial

resolution (500 *ppi* (point per inch)), were kept constant throughout the experiments. The surface pattern consists of linear cascades of rectangular areas. Each area is 4 mm×2.5 mm unless otherwise noted. The gradient is along the long edge of the rectangles. The pattern width was designed to ensure the droplets to be used in this study (with the volume of 10 μL to 60 μL) can always cover the entire pattern width.

To move the droplet along desired directions, the surface wettability should be within an appropriate range. If the surface is too hydrophilic, the droplet may stick on the substrate despite of high vibration frequency. If the surface is too hydrophobic, the droplet may move out of the pattern. After trial experiments, the operating parameters of $RI=-40\%$, and $n=4$ were used. GS equals 10% at the more hydrophobic edge and 18% at the more hydrophilic edge. After the treatments, the substrate was air blown and visually examined.

Surface wettability measurements

Three homogeneous substrates were prepared with constant GS values: 10%, 14%, and 18%. For all the three substrates, $RI=-40\%$ and $n=4$. The surface wettability of these substrates thus can represent the three different regions of a pattern with gradient surface wettability. In particular, the substrate with $GS=10\%$ represents the more hydrophobic edge within a pattern, the substrate with $GS=18\%$ represents the more hydrophilic edge within the same pattern, and the substrate with $GS=14\%$ represents the pattern center. Surface wettabilities of the substrates were measured by dispensing a 10 μL water droplet and performing contact angle measurements using a contact angle goniometer.

The anisotropic wettability was examined by tilting the substrates with gradient surface wettability along the transverse axis of the pattern and examining the minimal tilting angle that

can move a 20 μL droplet. The tilting angle increased from 0° with the increment of 1° . The stage was held still for 3 *sec* after each increment.

Droplet manipulation tests

After laser irradiation, the substrate was mounted on a customized stage and connected to a commercial vortex mixer (Maxi Mix II, Thermo Fisher Scientific, MA, USA). The stage translated the rotation motion generated by the vortex mixer into linear sinusoidal motion with the constant amplitude of ~ 4 *mm*. The frequency can be adjusted from 1 to 50 *Hz*. After a droplet was dispensed on the substrate, the motion of the droplet was recorded using a high-speed camera at 300 *fps* (Exilim Pro EX-F1, CASIO, Tokyo, Japan). Aqueous food color (Kroger, OH, USA) were added to the droplet at 5% *v/v* for better visualization.

Protein concentration measurements

The bicinchoninic acid (BCA) working reagent was prepared by mixing reagent *A* and the reagent *B* of Pierce BCA protein assay kit (Thermo Fisher Scientific, MA, USA) with a volumetric ratio of 50:1. The albumin stock solution provided by the kit was diluted by DI water to obtain the albumin solutions of different concentrations. These solutions were used to build a standard curve for albumin concentration quantification. After the reaction between albumin and BCA, the protein concentration was measured spectrophotometrically at 562 *nm* using a microplate reader (BioTek, VT, USA). A BCA assay following the standard protocol in a 96-well plate was performed as a control.

Statistical analysis

Student *t*-test was used to examine whether there were significant differences in the minimal sliding angles between different tiling directions and in the BCA reactions with different

protein concentrations. For the contact angle analysis, each group consisted of six measurements. For the sliding angle analysis, each group consisted of nine measurements. For the BCA assays, three samples in each group were characterized. The impact of the repeated water immersion on surface wettability was analyzed using one-way ANOVA. Statistical analyses were performed using JMP 11.0 (SAS®, NC, USA). $p < 0.05$ (*) is considered significant and $p < 0.01$ (**) is considered highly significant.

Results and Discussion

Characterization of Gradient Wettability

The static contact angle measurements show that the surface wettability increases with *GS* (**Fig. 2b**). The static contact angle is $152.5 \pm 2.8^\circ$ under $GS=10\%$; $137.2 \pm 1.8^\circ$ under $GS=14\%$; and $125.7 \pm 3.4^\circ$ under $GS=18\%$. The static contact angle of an unmodified super-hydrophobic substrate is $\sim 165^\circ$. It confirms that laser irradiation with spatially variable laser power can create gradient surface wettability.

The entire surface was kept within the hydrophobic regime with the static water contact angle $> 125^\circ$. This helped to reduce surface fouling and cross-contamination, a critical concern for biochemical assays. To validate this, a $10 \mu\text{L}$ droplet stained with 0.1% rhodamine B (Sigma Aldrich, MO, USA) was dispensed on the working surfaces treated by varied laser parameters. After 10 sec, the droplet was removed and the surfaces were examined by fluorescence microscopy. The results showed that the surface treated with $GS=18\%$, $RI=-40\%$, and $n=4$ (representing the most hydrophilic areas in the patterns) had significantly lower fluorescence intensity compared to the surfaces with smaller static water contact angles (Section 3 in ESI).

The sustainability of surface wettability in aqueous medium and in air were examined. Three

groups of samples were prepared to represent the more hydrophilic edge ($GS=18\%$) and the more hydrophobic edge ($GS=10\%$). $RI=-40\%$ and $n=4$ for all the samples. The samples were immersed in water and withdrew from water for up to 1000 times to have the waterline pass the surfaces repeatedly. Static water contact angle was examined after the tests. One-way ANOVA (with the confidence level of 95%) showed that the time of repeated water immersion does not cause significant difference in the contact angle for all the samples. The water contact angle of the samples exposed for about two years in air was measured and compared to as-prepared samples treated with the same parameters. No significant difference of surface wettability was detected (Section 4 in ESI).

The surface with gradient wettability exhibits anisotropic minimal sliding angles (**Fig. 2c**): the minimal sliding angle for the droplet to move towards the forward direction is $36.71 \pm 3.1^\circ$, while that towards the backward direction is $53.29 \pm 3.7^\circ$. The minimal sliding angles along the opposite directions are significantly different from each other. For comparison, the minimal sliding angle of the droplet on the non-irradiated super-hydrophobic substrate is $2.75 \pm 0.5^\circ$. This suggests that the minimal inertial forces that can displace the droplets along the opposite directions are different, which makes it possible to induce unidirectional droplet motion using symmetric in-plane vibration.

Long-distance droplet translocation

Long-distance droplet translocation was demonstrated. A $20 \mu\text{L}$ droplet was dispensed at the distal end of the repeated patterns (**Fig. 3a** and **Movie 1**). The vibration frequency ramped up from 1 Hz . At a low frequency, the droplet vibrated but did not displace on the surface. Once the vibration frequency exceeded $\sim 8 \text{ Hz}$, the droplets moved towards the forward direction and reached the pattern edge within one cycle. In other words, the droplet traveled the distance that

equals to pattern length within a cycle. With the vibration amplitude $A_0 = 4 \text{ mm}$ and the vibration frequency $f = 10 \text{ Hz}$, the droplet traveled over a distance of 16 mm within 400 ms , corresponding to the traveling speed of $\sim 40 \text{ mm/s}$ (**Movie 2**). For comparison, a droplet dispensed within the area with homogenous laser irradiation dose ($GS = 18 \%$, $RI = -40\%$, and $n = 4$) vibrated around the original spot and did not exhibit a net displacement upon continuous cyclic vibration.

Long-distance droplet motion along a pre-determined two-dimensional trajectory was also demonstrated. The traveling path as illustrated in **Fig. 3b** was patterned on the substrate, which consisted of four linear cascades of repeated patterns with gradient surface wettability that connected head-to-tail to each other into a square shape. Each cascade is 16 mm long. A $20 \mu\text{L}$ droplet was dispensed to a corner of the path (Corner 1). Upon the vibration at $\sim 9 \text{ Hz}$ along the longitudinal direction of the first cascade, the droplet moved towards Corner 2. Subsequent cyclic vibrations along the transverse and longitudinal directions further moved the droplet to Corner 3, Corner 4, and eventually back to Corner 1 (**Movie 3**).

Moving a droplet along an arbitrary patterned path using circular agitation is also possible. This was done by mounting the substrate directly on the vortex mixer without using the customized stage. To prevent the droplets from moving off the patterns, a higher hydrophobicity barrier between the untreated areas and the more hydrophobic edge of the patterns ($GS = 14\%$, $RI = -40\%$, and $n = 4$) was built. The more hydrophilic edge of the patterns was kept the same as above ($GS = 10\%$, $RI = -40\%$, and $n = 4$). A $20 \mu\text{L}$ droplet was dispensed on a cascade of patterns ($4 \text{ mm} \times 1.5 \text{ mm}$). A circular agitation of $\sim 400 \text{ rpm}$ was applied. The droplet travelled over the distance of 16 mm within 0.7 sec without transverse movement off the patterns (**Movie 4**).

Droplet mixing

Mixing of two droplets is an essential function of open channel microfluidics and is used extensively for biochemical analysis^{18, 26, 27}. In this study, droplet mixing was performed by aligning two linear cascades of gradient surface wettability patterns with each other while having their more hydrophobic edges meet in a central square area ($4\text{ mm} \times 4\text{ mm}$) (**Fig. 3c**). The square area was engraved with $GS=25\%$. Two $20\ \mu\text{L}$ droplets stained with different colors (blue and yellow) were dispensed at the distal ends of the two opposite cascades. They were 28 mm apart from each other. Once the in-plane vibration of 10 Hz was applied, both droplets moved towards the square area at the center and met with each other within $\sim 300\text{ ms}$ (**Movie 5**). The in-plane vibration not only brought the two droplets together but also enhanced the droplet mixing efficiency. The color of the mixed droplet became homogeneous within 2.5 sec , corresponding to 25 vibration cycles. It, however, took more than 30 sec to thoroughly mix two droplets of the same volumes without vibration (**Fig. 3d**).

Selective movement of multiple droplets with different volumes

The second term on the left of **Eqn. 1** can be expressed using Taylor series expansion. The acceleration associated with the drag force can be expressed as:

$$\frac{\gamma C w (\cos \theta_r - \cos \theta_a)}{m} = k_1 \frac{w}{V} + k_2 w V^{1/3} + k_3 \frac{w}{V^{2/3}} \quad (4),$$

where $k_1 = 1.340 \frac{\gamma C}{\rho}$, $k_2 = 0.017 \frac{\gamma C}{\rho L^2}$ and $k_3 = 0.059 \frac{\gamma C}{\rho L}$. k_1 , k_2 and k_3 are the coefficients determined by experimentally measured dynamic contact angles, ρ is the droplet density, and V is the droplet volume. It is seen that the acceleration associated with the drag force varies with the droplet volume and the pattern width (**Fig. 4a**). In particular, the acceleration increases with the pattern width, and decreases with the increase of the droplet volume. With a given volume, a larger inertial force is required to move a droplet on a wider pattern. As a

consequence, the minimal frequency that can accelerate the droplet on a wider pattern is higher. Similarly, with a given pattern width, a smaller inertial force, and therefore a lower minimal frequency, is required to move a larger droplet. The changes of minimally required frequency with the droplet volume and the pattern geometries were experimentally validated (**Table 1**). For the smallest droplet we used in this study (about $2 \mu\text{L}$), the driving frequency needed to be at 42Hz or higher to move the droplet on a cascade of $4\text{mm} \times 2.5\text{mm}$ patterns. The minimal driving frequency dropped to 11Hz when the patterns changed to $3.5\text{mm} \times 1.5\text{mm}$.

Because the minimally required frequency to accelerate the droplet varies with the pattern width and the droplet volume, selective droplet manipulation is possible by placing droplets of the same volumes on gradient wettability patterns of different widths or placing droplets of different volumes on gradient wettability patterns of the same widths. An experiment was performed to demonstrate both cases. Two cascades of linear patterns with gradient surface wettability were connected head-to-tail. The patterns in the first cascade are $4 \text{ mm} \times 2.5 \text{ mm}$ in dimension, and the patterns in the second cascade are $4 \text{ mm} \times 3 \text{ mm}$ in dimension. The total lengths of the first and the second cascades are 12 mm and 8 mm , respectively. The more hydrophobic end of the second cascade was connected to a square ($4\text{mm} \times 4\text{mm}$) that had been irradiated by a laser with $GS=25 \%$ (**Fig. 4b**). A $20 \mu\text{L}$ droplet was dispensed on the more hydrophilic end of the first cascade, and another $20 \mu\text{L}$ droplet was dispensed on the more hydrophilic end of the second cascade. Upon 10 Hz cyclic vibration, the droplet on the first cascade moved towards the forward direction, while the droplet on the second cascade kept stationary. Once the moving droplet reached the second cascade and met with the stationary droplet, the merged droplet gained the volume of $40 \mu\text{L}$. The merged droplet then moved further towards the forward direction and eventually reached the square on the right.

Selective manipulation of an array of droplets on the same substrate was also demonstrated (**Movie 6**). Three droplet traveling paths were patterned on the substrate (**Fig. 4c**). The first path consisted of a linear cascade made up of rectangular patterns. Each pattern is $4\text{mm} \times 2.5\text{mm}$ in dimension and has gradient surface wettability as above described. The length of the first cascade is 12 mm . The second path consisted of two linear cascades made up of rectangular patterns. The patterns in the first cascade are $4\text{mm} \times 2.5\text{mm}$ and the patterns in the second cascade are $4\text{mm} \times 3\text{mm}$. The length of the first cascade is 12 mm , and the length of the second cascade is 8 mm . The third path consisted of three linear cascades made up of rectangular patterns. The patterns in the first cascade are $4\text{mm} \times 2.5\text{mm}$, the patterns in the second cascade are $4\text{mm} \times 3\text{mm}$, and the patterns in the third cascade are $4\text{mm} \times 3.5\text{mm}$. The lengths of the first, second, and the third cascades are 12 mm , 8 mm , and 8 mm , respectively. The more hydrophobic ends of all the three paths were connected to a square ($4\text{ mm} \times 4\text{ mm}$) that had been irradiated by a laser with $GS=25\%$. Six $20\text{ }\mu\text{L}$ droplets were dispensed within the three paths as shown in **Fig. 4d**, where the droplets resided in the area with the pattern width of 2.5 mm , 3 mm , and 3.5 mm were stained with yellow, blue and red colors, respectively. Upon 10 Hz cyclic vibration, yellow droplets first moved towards the forward direction. The droplets in the second and the third paths met with the blue droplets. The merged droplets ($40\text{ }\mu\text{L}$) then moved further towards the forward direction. The merged droplet in the third path further met with the red droplet. After merging, the resulting droplet gained $60\text{ }\mu\text{L}$ in volume. The $60\text{ }\mu\text{L}$ droplet did not exhibit a large displacement upon 10 Hz vibration. This is probably because the frequency is well above the appropriate range (f_{max}) so that the viscosity dissipation induced damping effect becomes predominant. The $60\text{ }\mu\text{L}$ droplet can be moved by lowering the frequency to $\sim 5\text{ Hz}$. Finally, all the droplets were collected in the squares on the right (**Fig. 4e**). The time-lapse movement of the droplets in the third path is shown in **Fig. 4f**.

Protein concentration measurement

The efficacy of this droplet manipulation approach for biochemical analysis was demonstrated through the measurement of albumin concentration in a sample solution. Five droplet paths were patterned on the PDMS substrate. Each path consists of two rectangular areas with gradient surface wettability. Similar as in the above experiments, each rectangular area is $4\text{ mm} \times 2.5\text{ mm}$, and the GS within each area ranged from 10 % to 18 %. The length of each path is 8 mm . The more hydrophobic ends of all the paths were connected to squares that were $4\text{ mm} \times 4\text{ mm}$ each and engraved with $GS=25\%$ (**Fig. 5a**). Among the five paths, three were used to provide the calibration curve (refers to the calibration paths), one served as a control (refers to the control path), and the rest one was used to host the reaction of the sample with an unknown protein concentration (refers to the measurement path). A $10\mu\text{L}$ droplet with albumin concentration of 0, 250, 500, and $1000\mu\text{g/mL}$ was dispensed within the squares of the control path and the three calibration paths, respectively, and dried. A $2\mu\text{L}$ droplet with an unknown albumin concentration was dispensed on the square of the measurement path. A $20\mu\text{L}$ droplets of BCA working reagent was dispensed to the more hydrophilic end of each path. Upon 10 Hz vibration, the BCA droplets moved to the squares within 2 sec . The substrate was continuously vibrated to allow thorough mixing of the BCA reagents and albumin. The substrate was kept at $37\text{ }^\circ\text{C}$. As the BCA droplets reacted with albumin, the droplets changed their colors. The albumin concentration in the measurement path was determined by measuring the light absorbance at 562 nm and compared with those in the control and calibration paths. The volume difference between the measurement path and the control/calibration paths were compensated using the Beer-Lambert law. In particular, a standard calibration curve with a high regression coefficient > 0.987 was obtained (**Fig. 5b**). The albumin concentration of the merged droplet in the measurement path was calculated as $236 \pm 5.9\mu\text{g/mL}$ (the red dot). The albumin

concentration of the original 2 μL droplet was calculated as $2360 \pm 59 \mu\text{g}/\text{mL}$. The difference between the measurement using the droplet-based assay and that by the standard BCA assay ($232 \pm 10.5 \mu\text{g}/\text{mL}$) was within the measurement error.

The droplet-based analysis used 20 μL BCA reagents in each path, which was significantly lower than those in a standard BCA assay performed using 96-well plates (200 μL in each well)³⁹. The reaction time was also significantly reduced. In the droplet-based analysis, the light absorbance reached 95 % of its maximum within 10 *min*, while it took more than 30 *min* for a standard BCA assay to reach the same (**Fig. 5c**). The faster reaction time was also observed for measurements performed at the room temperature (25°C), where the droplet-based analysis achieved 95 % of maximal light absorbance within 20 *min* (blue line in **Fig. 5d**), while the standard BCA assay needed more than 120 *min* to reach the same (red line in **Fig. 5d**). The droplet-based analysis without post-mixing vibration was also performed at the room temperature, which reached 95% light absorbance less than 90 *min* (green line in **Fig. 5d**). Collectively, the reaction time reduction is believed due to both the small sample volume and the continuous in-plane vibration.

The minimally detectable concentration of droplet-based analysis was investigated by measuring highly diluted albumin solutions with the concentration down to 0.625 $\mu\text{g}/\text{mL}$. The result shows that using 20 μL BCA droplets and 2 μL sample droplets, the minimally detectable protein concentration was 5 $\mu\text{g}/\text{mL}$ (blue line in **Fig. 5e**). This is similar to the minimally detectable protein concentration of standard BCA assays (red line in **Fig. 5e** and ³⁹).

Conclusion

In this paper, we report an approach to move droplets on an open surface by arranging repeated

patterns with gradient surface wettability and applying symmetric in-plane vibration. The surface wettability ranged from $152.5 \pm 2.8^\circ$ to $125.7 \pm 3.4^\circ$ within one pattern by decomposing a super-hydrophobic coating using laser irradiation of varied doses. Due to the gradient surface wettability and the head-to-tail arrangement of repeated patterns, the minimal vibration frequencies that can move a droplet towards opposite directions are different. An analytical model was developed to investigate the droplet motion. The vibration frequency range that can displace the droplets was determined. The model also reveals that the minimal frequency that can move the droplets is a function of the droplet volume and the pattern width. This makes it possible to move selected droplets while keeping others stationary. Using a vortex mixer that is commonly accessible in biochemical laboratories, symmetric in-plane vibration was generated. Long-distance droplet movement along a pre-determined trajectory, droplet mixing, and selective manipulation of multiple droplets were implemented. The protein concentration measurement shows that this approach has the comparable measurement accuracy with conventional BCA assays, but has a faster reaction rate, and reduced reagent consumption. This approach provides a new scheme to perform the droplet-based experiments and analyses with little surface fouling. The controlled droplet manipulation with low technical barrier and easy operation is expected to broaden the applications of open microfluidics for applications in biochemistry, pharmacology, and microbiology.

Acknowledgement

This study is partially supported by National Science Foundation through a grant 1509727 and a facility grant provided by Institute for Materials Research at The Ohio State University.

Conflict of Interests

There is no conflict of interests to declare.

References:

1. T. Konry, S. S. Bale, A. Bhushan, K. Shen, E. Seker, B. Polyak and M. Yarmush, *Mikrochimica acta*, 2012, **176**, 251-269.
2. P. S. Dittrich and A. Manz, *Nat Rev Drug Discov*, 2006, **5**, 210-218.
3. H. Song, D. L. Chen and R. F. Ismagilov, *Angewandte Chemie*, 2006, **45**, 7336-7356.
4. X. Casadevall i Solvas and A. deMello, *Chem Commun (Camb)*, 2011, **47**, 1936-1942.
5. S. Y. Teh, R. Lin, L. H. Hung and A. P. Lee, *Lab Chip*, 2008, **8**, 198-220.
6. A. B. Theberge, F. Courtois, Y. Schaerli, M. Fischlechner, C. Abell, F. Hollfelder and W. T. Huck, *Angewandte Chemie*, 2010, **49**, 5846-5868.
7. D. J. Shin and T.-H. Wang, *Annals of biomedical engineering*, 2014, **42**, 2289-2302.
8. W. Feng, E. Ueda and P. A. Levkin, *Advanced materials*, 2018, **30**, 1706111.
9. W. C. Nelson and C.-J. C. Kim, *J Adhes Sci Technol*, 2012, **26**, 1747-1771.
10. Y. Zhao and S. K. Cho, *Lab Chip*, 2007, **7**, 273-280.
11. W. Satoh, H. Hosono and H. Suzuki, *Anal Chem*, 2005, **77**, 6857-6863.
12. Y. Fouillet, D. Jary, C. Chabrol, P. Claustre and C. Peponnet, *Microfluid Nanofluid*, 2008, **4**, 159-165.
13. J. Lee, H. Moon, J. Fowler, T. Schoellhammer and C. J. Kim, *Sensor Actuat a-Phys*, 2002, **95**, 259-268.
14. M. Mibus, C. Jensen, X. Hu, C. Knospe, M. L. Reed and G. Zangari, *J Appl Phys*, 2013, **114**.
15. H. H. Shen, L. Y. Chung and D. J. Yao, *Biomicrofluidics*, 2015, **9**.
16. S. Choi, Y. Kwon, Y.-S. Choi, E. S. Kim, J. Bae and J. Lee, *Langmuir*, 2012, **29**, 501-509.
17. H. Geng, J. Feng, L. M. Stabryla and S. K. Cho, *Lab Chip*, 2017, **17**, 1060-1068.
18. C. Yang and G. Li, *Scientific reports*, 2017, **7**, 15705.
19. K. Katoh, H. Tamura, E. Sato and T. Wakimoto, *Exp Fluids*, 2018, **59**.
20. S. Biswas, Y. Pomeau and M. K. Chaudhury, *Langmuir*, 2016, **32**, 6860-6870.
21. A. A. Darhuber, J. P. Valentino, J. M. Davis, S. M. Troian and S. Wagner, *Appl Phys Lett*, 2003, **82**, 657-659.
22. S. C. S. Lin, X. L. Mao and T. J. Huang, *Lab Chip*, 2012, **12**, 2766-2770.
23. K. A. Wier, L. C. Gao and T. J. McCarthy, *Langmuir*, 2006, **22**, 4914-4916.
24. C. J. Huang, W. F. Fang, M. S. Ke, H. Y. E. Chou and J. T. Yang, *Lab Chip*, 2014, **14**, 2057-2062.
25. S. Daniel, M. K. Chaudhury and P. G. de Gennes, *Langmuir*, 2005, **21**, 4240-4248.
26. L. Y. Yeo and J. R. Friend, *Biomicrofluidics*, 2009, **3**, 012002.
27. T. Kong, R. Brien, Z. Njus, U. Kalwa and S. Pandey, *Lab Chip*, 2016, **16**, 1861-1872.
28. L. Dong, A. Chaudhury and M. K. Chaudhury, *Eur Phys J E*, 2006, **21**, 231-242.
29. M. K. Chaudhury and G. M. Whitesides, *Science (New York, N.Y.)*, 1992, **256**, 1539-1541.
30. A. Shastry, M. J. Case and K. F. Böhringer, *Langmuir*, 2006, **22**, 6161-6167.
31. S. Daniel, S. Sircar, J. Gliem and M. K. Chaudhury, *Langmuir*, 2004, **20**, 4085-4092.

32. S. Daniel and M. K. Chaudhury, *Langmuir*, 2002, **18**, 3404-3407.
33. H. R. Holmes and K. F. Böhringer, *Microsystems & Nanoengineering*, 2015, **1**, 15022.
34. T. A. Duncombe, E. Y. Erdem, A. Shastry, R. Baskaran and K. F. Bohringer, *Advanced materials*, 2012, **24**, 1545-1550.
35. H. R. Holmes, A. E. Gomez and K. F. Böhringer, 2016.
36. A. Shastry, D. Taylor and K. F. Bohringer, presented in part at the Solid-State Sensors, Actuators and Microsystems Conference, TRANSDUCERS, 2007.
37. T. A. Duncombe, J. F. Parsons and K. F. Bohringer, *Langmuir*, 2012, **28**, 13765-13770.
38. L. Qi, C. Ruck, G. Spychalski, B. King, B. Wu and Y. Zhao, *Acs Appl Mater Inter*, 2018, **10**, 4295-4304.
39. ThermoScientific, *User Guide: Pierce BCA Protein Assay Kit (MAN0011430 Rev. A)*, 2013.

Figures:

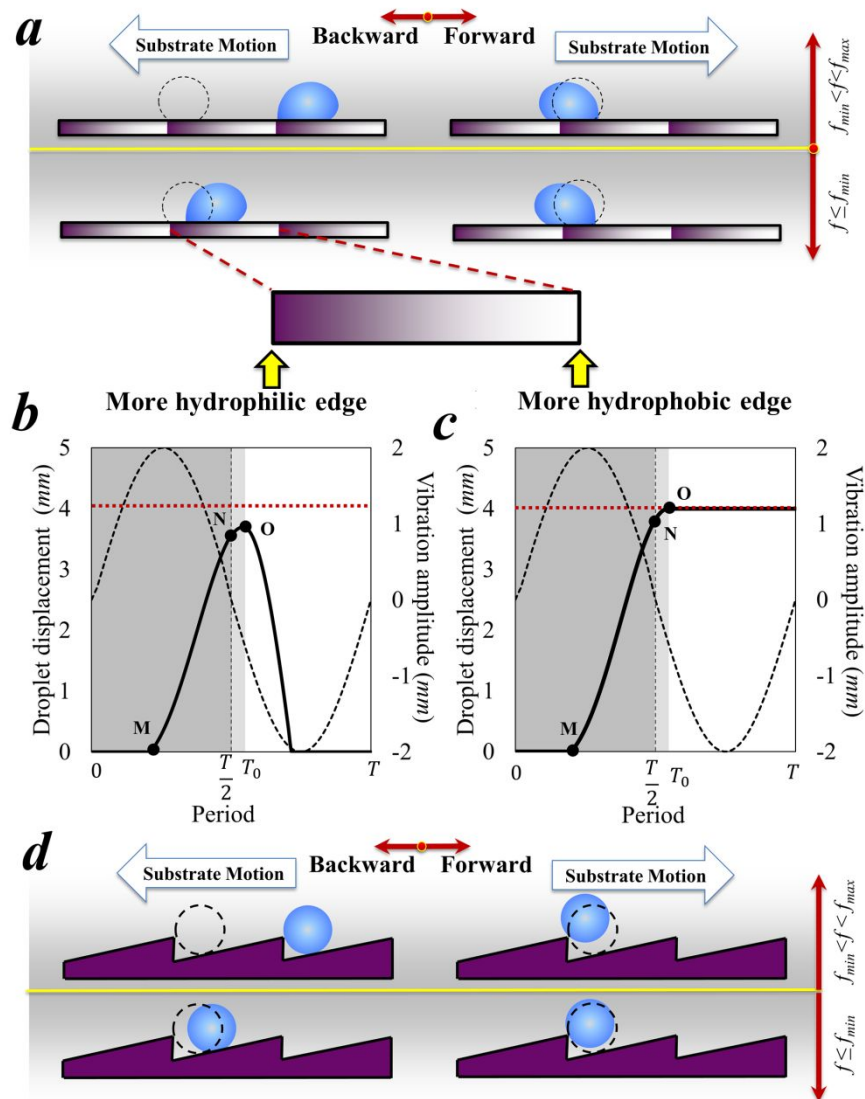


Figure 1. Droplet manipulation principle. (a) Schematic of the droplet motion on a gradient wettability surface under in-plane vibration; (b) The calculated displacement of a 20 μL droplet under 8 Hz vibration. The droplet is not able to reach the next pattern within one vibration cycle; (c) The calculated displacement of a 20 μL droplet under 8.87 Hz vibration. The droplet exhibits a total displacement equaling to the pattern length (4 mm) within one vibration cycle; and (d) Schematic of a rigid sphere moving on repeated saw-toothed patterns for analogy.

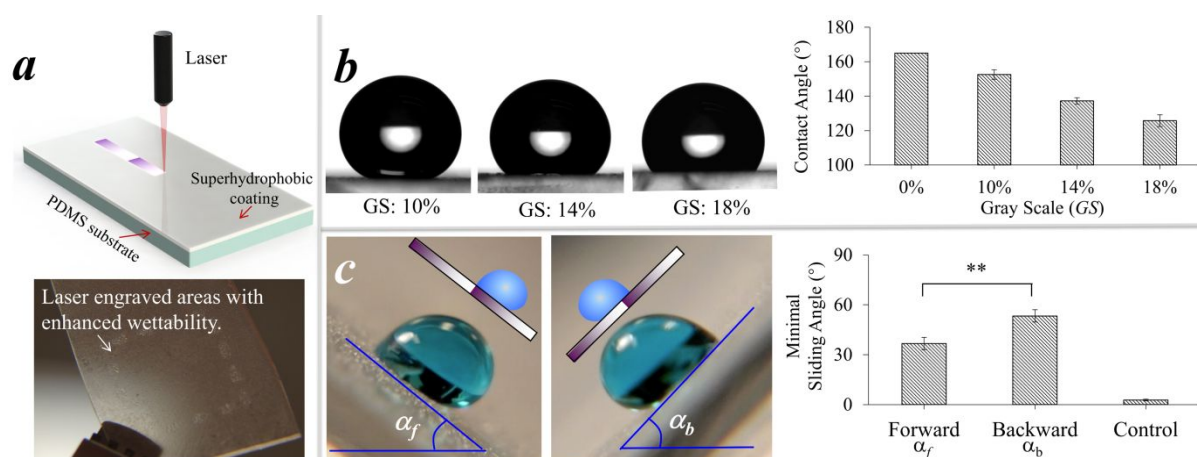


Figure 2. Fabrication of surface patterns with gradient wettability. (a) The superhydrophobic layer was irradiated by a laser engraver with spatially varying power. (b) Contact angle measurements on a laser irradiated surface using a $10 \mu\text{L}$ droplet. (c) The anisotropic minimal sliding angle towards the forward and the backward directions. The control group refers to the minimal sliding angle measurement on a super-hydrophobic surface not subject to laser irradiation.

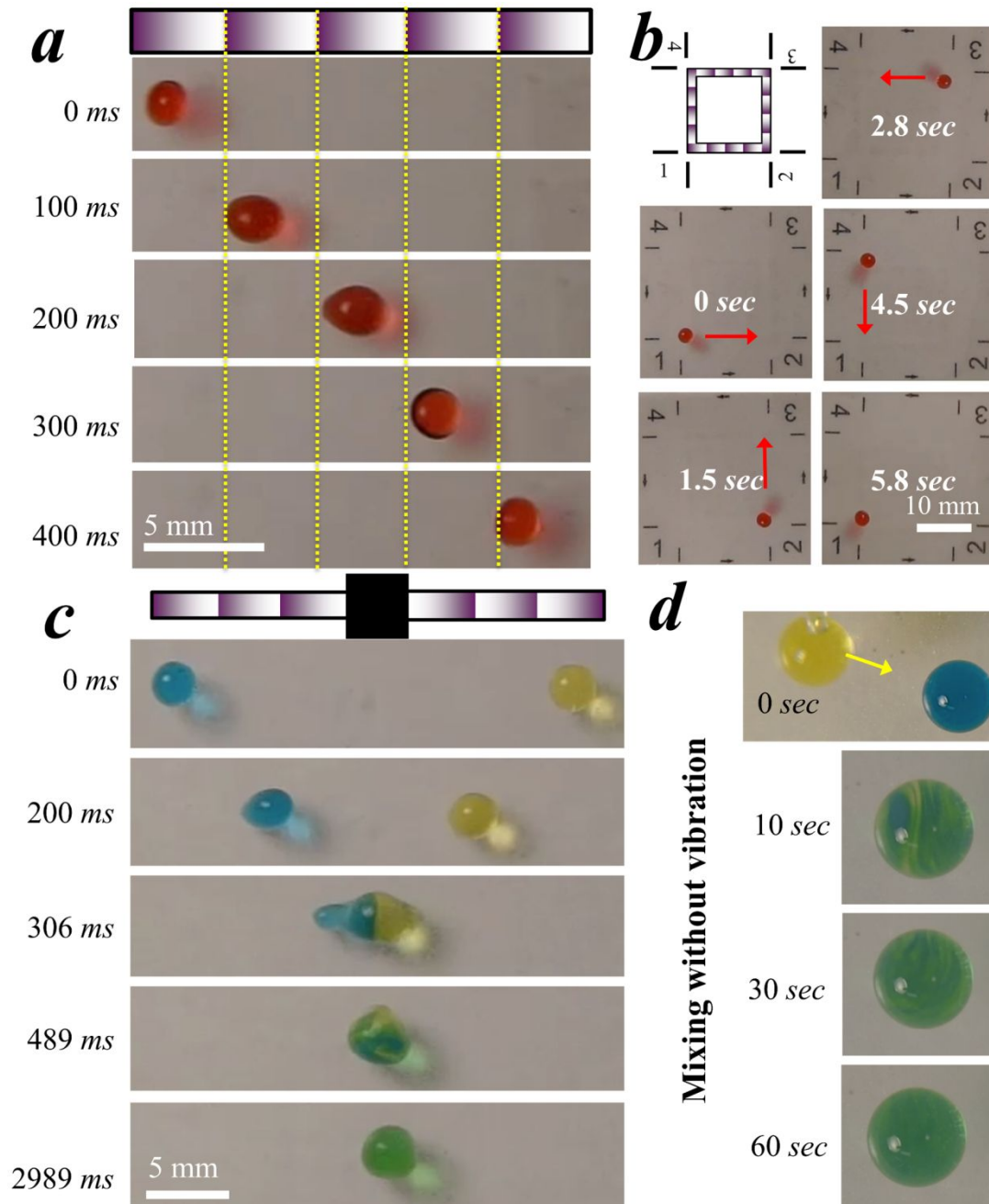


Figure 3. Long distance droplet movement. (a) Long-distance droplet translocation on a linear pattern cascade (**Movie 2**). (b) Droplet motion along a pre-determined two-dimensional trajectory (**Movie 3**). (c) Droplet mixing by moving two droplets toward opposite directions, and (d) Droplet mixing without vibration (**Movie 5**).

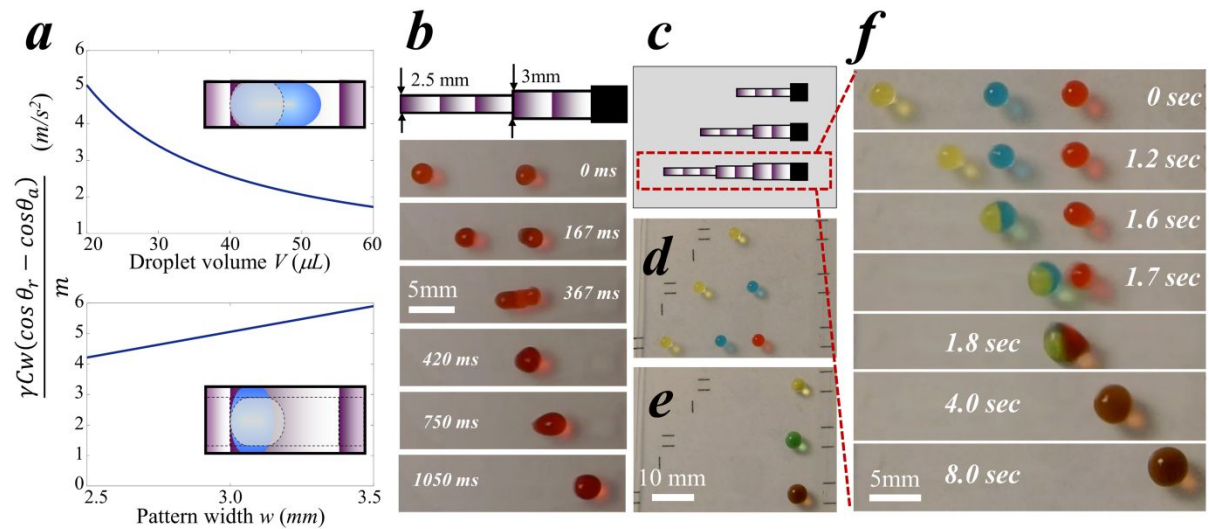


Figure 4. Selective droplet manipulation. (a) The effects of the droplet volume and the pattern width on the acceleration associated with the contact angle hysteresis ($\frac{\gamma C w (\cos \theta_r - \cos \theta_a)}{m}$). (b) Selective manipulation of two droplets on linear patterns. The pattern widths of the left and the right segments were 2.5 mm and 3 mm, respectively. (c-f) Selective manipulation of an array of droplets on the same substrate (**Movie 6**): (c) the pattern design; (d&e) the droplet positions before and after manipulation; and (f) the time-lapse images of droplets in the third path.

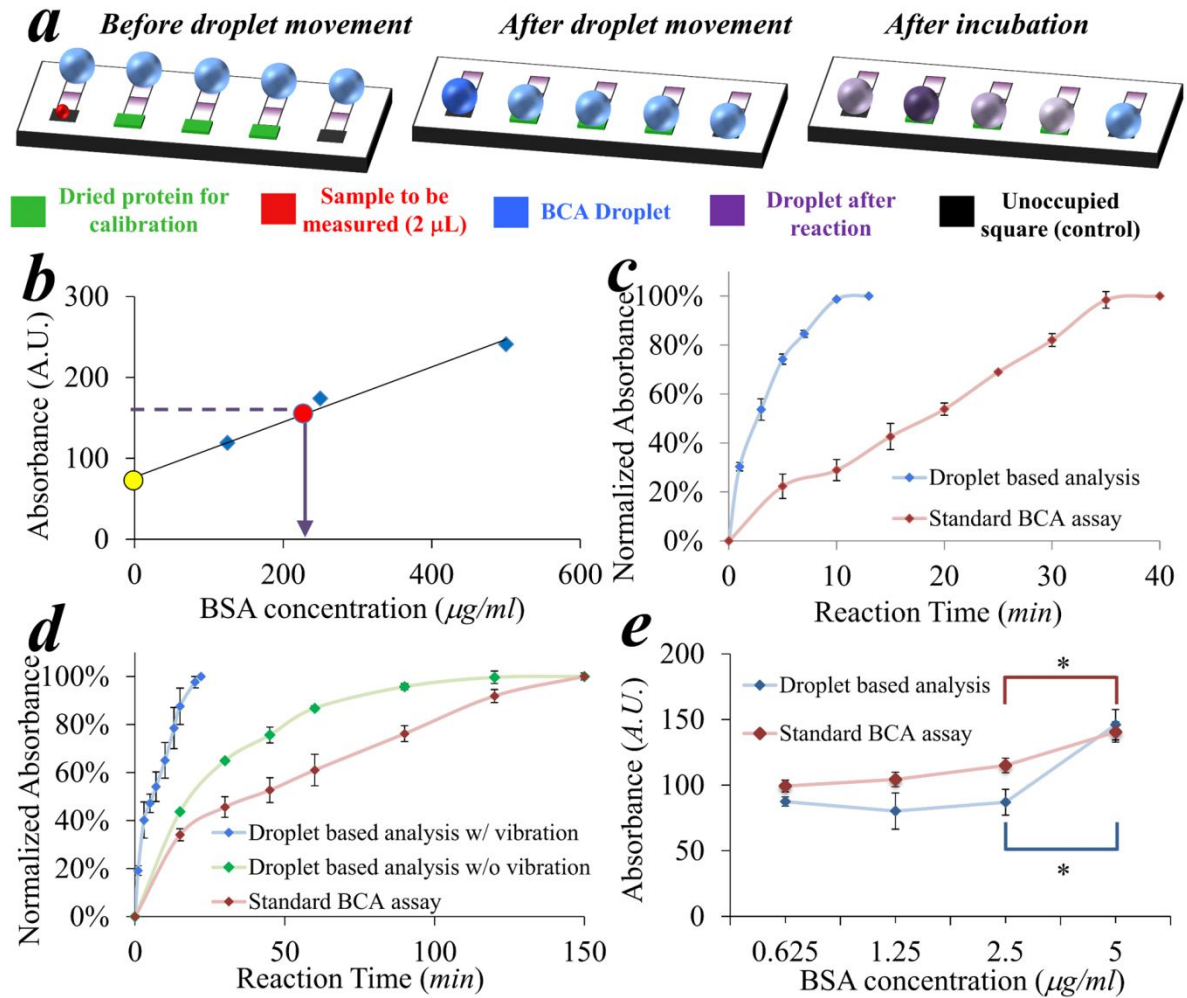


Figure 5. Droplet-based protein measurements. (a) Schematic of the device and the measurement procedure. Multiple calibration paths, the measurement path and the control path were arranged in parallel. (b) The light absorbance of the droplets: The blue diamonds denote the measurements from the calibration path; the yellow circle denotes the measurement from the control path; and the red circle denotes the measurement of the unknown sample. (c&d) Comparison of the reaction rates between the droplet-based measurement and a standard BCA assay in a 96-well plate. (c) was obtained at 37°C and (d) was obtained at the room temperature. The reaction rate using the device without vibration was examined as a control group in (d). (e) Comparison of the minimally measurable albumin concentrations by the two methods.

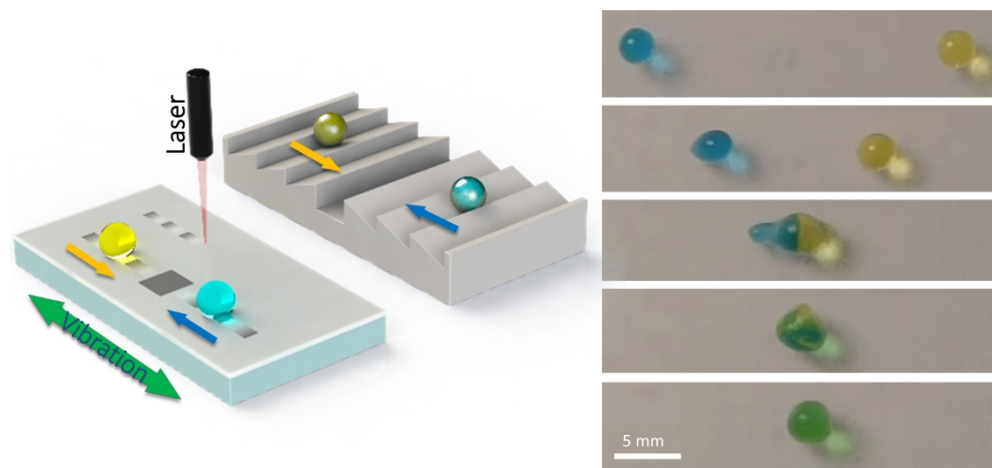
Tables

Minimal Vibration Frequency (<i>Hz</i>)			
Pattern Dimension (L × W)	4 mm × <u>2.5 mm</u>	4 mm × <u>3 mm</u>	4 mm × <u>3.5 mm</u>
Droplet Volume (<i>mL</i>)			
15	11	13	13
20	10	12	12
25	8	10	11
30	7	9	9
40	7	8	9
60	-	1	2

Table 1: The relationship of minimal vibration frequency with droplet volume and pattern width.

Table of Content

Long-distance droplet motion and selective droplet manipulation on repeated hydrophobic surface patterns with gradient wettability by in-plane cyclic vibration.



319x159mm (300 x 300 DPI)